Optics Letters

Amorphous-silicon visible-light detector integrated on silicon nitride waveguides

Christian De Vita,[1,*] Fabio Toso,[1] Natale Giovanni Pruiti,[2] Charalambos Klitis,[2] Giorgio Ferrari,[1] Marc Sorel,[2,3] Andrea Melloni,[1] and Francesco Morichetti[1]

[1]Dipartimento di Elettronica, Informazione e Bioingegneria (DEIB), Politecnico di Milano, 20133, Italy
[2]University of Glasgow, Rankine Building, Oakfield Avenue, Glasgow G12 8LT, UK
[3]TeCIP Institute, Scuola Superiore Sant'Anna, 56124 Pisa, Italy
*Corresponding author: christian.devita@polimi.it

Received 4 February 2022; revised 4 April 2022; accepted 18 April 2022; posted 22 April 2022; published 13 May 2022

Visible-light integrated photonics is emerging as a promising technology for the realization of optical devices for applications in sensing, quantum information and communications, imaging, and displays. Among the existing photonic platforms, high-index-contrast silicon nitride (Si_3N_4) waveguides offer broadband transparency in the visible spectral range and a high scale of integration. As the complexity of photonic integrated circuits (PICs) increases, on-chip detectors are required to monitor their working point for reconfiguration and stabilization operations. In this Letter, we present a semi-transparent in-line power monitor integrated on Si_3N_4 waveguides that operates in the red-light wavelength range (660 nm). The proposed device exploits the photoconductivity of a hydrogenated amorphous-silicon (a-Si:H) film that is evanescently coupled to an optical waveguide. Experimental results show a responsivity of 30 mA/W, a sensitivity of –45 dBm, and a sub-μs time response. These features enable the use of the proposed photoconductor for high-sensitivity monitoring and control of visible-light Si_3N_4 PICs.

https://doi.org/10.1364/OL.455458

Visible light is a spectral region that is attracting increasing interest in many applications, including data communications [1], microscopy [2], biosensing [3], nanomedicine [4,5], quantum optics [6,7], and virtual reality [8]. In this wavelength range, silicon nitride (Si_3N_4) is one of the most established high-index-contrast platforms for photonic integrated circuits (PICs) because it offers a good trade-off between low propagation loss and high integration scale [9]. As in the near-infrared range, the realization of visible-light reconfigurable and programmable PICs [10] requires the integration of various photonic components on a single chip, including light sources and detectors. On-chip detectors are essential to monitor the working point of the PIC in order to set and stabilize its functionality by using closed-loop control tools. Different strategies have been recently proposed for the integration of visible-light photodetectors in Si_3N_4 waveguides. Monolithic integration of a p-i-n silicon photodiode at 488 nm has been demonstrated by exploiting vertical evanescent coupling between a Si_3N_4 waveguide and a crystalline silicon (c-Si) waveguide in a two-waveguide-layer silicon photonics platform [11]. Wideband avalanche photodetectors at 685 nm have been monolithically integrated by end-fire coupling of a Si_3N_4 waveguide and a c-Si waveguide [12]. Although providing good performance in terms of responsivity and speed, these approaches require complex technological steps to be performed on a pre-existing c-Si waveguide platform and cannot be ported onto a conventional Si_3N_4 platform. Alternative options include the heterogeneous integration of Si or III-V compounds photodetectors, which require higher costs of fabrication and assembly [13]. Hydrogenated amorphous-silicon (a-Si:H) is widely used in the visible range for thin-film light detectors, such as in photovoltaic applications, but its use in integrated optics is rather limited. By introducing hydrogen during the a-Si deposition, dangling bonds are reduced and photoconductivity is significantly improved [14]. The integration of an a-Si detector on a lithium niobate on Si waveguide has been recently demonstrated at 850 nm wavelength [15].

In this Letter, we exploit the photoconductivity of an a-Si:H film deposited as a coating layer of a Si_3N_4 waveguide to realize a monolithically integrated compact in-line photoconductor operating in the red-light range. In order to realize a semi-transparent detector, the a-Si:H film is evanescently coupled to the Si_3N_4 core by means of an intermediate spacing layer enabling controllable absorption of the guided mode.

Figure 1(a) shows a schematic of the proposed device. The detector is integrated on a channel Si_3N_4 waveguide with a core thickness of 200 nm cladded with a 600-nm thick layer of hydrogen silsesquioxane (HSQ) (see Supplement 1 for details on the fabrication process). The waveguide width $w = 400$ nm guarantees single-mode propagation down to a wavelength of 630 nm. The HSQ layer is locally lowered to a thickness h_c in order to guarantee the proper overlap of the optical mode with the a-Si top layer. Numerical simulations based on the Beam Propagation Method (BPM) were carried out to evaluate the absorption of the a-Si layer versus the gap distance h_c. As refractive indices of SiO_2 and Si_3N_4 at a wavelength of 660 nm, we used data available in the literature ($n_{Si3N4} = 2.007$ [16] and $n_{SiO2} = 1.471$

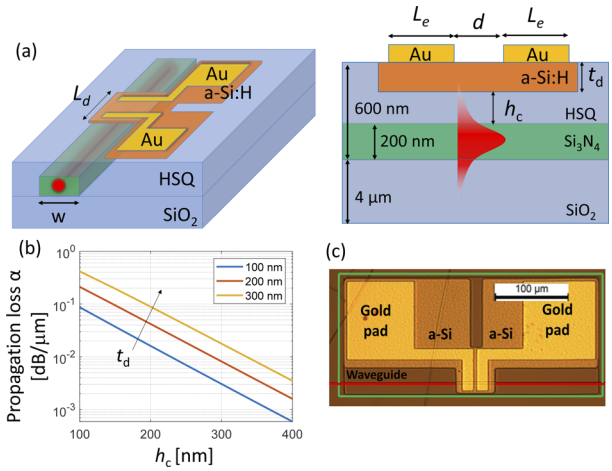

Fig. 1. (a) Schematics of the a-Si photoconductor integrated in a Si_3N_4 waveguide; (b) simulated propagation loss versus the spacing h_c between a-Si:H film and the Si_3N_4 core for different thicknesses t_d of the a-Si:H film; (c) top view optical microscope image of one of the fabricated devices.

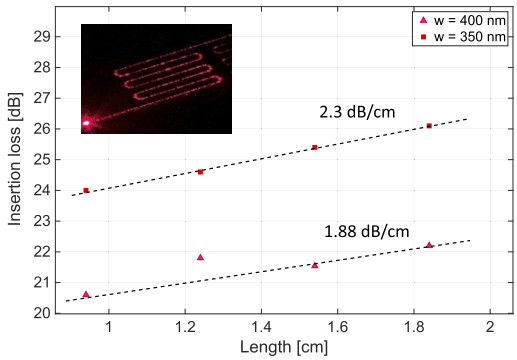

Fig. 2. Measured propagation losses at a wavelength of 660 nm of single-mode Si_3N_4 waveguides with a width of 350 nm (red squares) and 400 nm (magenta triangles). Inset: photo of the chip coupled with a red-light source.

[17]); the refractive indices and extinction coefficients of the a-Si and the cured HSQ were measured by using spectroscopic ellipsometry on test films, resulting respectively in $n_{HSQ} = 1.40$, $n_{a-Si} = 3.60$ and $k_{HSQ} < 10^{-3}$, $k_{a-Si} = 0.05$ at wavelength 660 nm. Figure 1(b) shows the simulated propagation loss α of the fundamental transverse electric (TE) guided mode versus h_c for different a-Si thicknesses t_d. The choice of h_c is a trade-off between device footprint, insertion loss, and responsivity of the detector. Using $t_d = 200$ nm and $h_c = 200$ nm (α= 0.04 dB/µm), an in-line detector with an overall length $L_d = 50$ µm and 2 dB light absorption is achieved. Simulations show that discontinuities at the input/output sections of the detector introduce less than 1% loss per transition and back reflections smaller than –50 dB, so that no adiabatic mode adapters are required.

Figure 1(c) shows a top view optical microscope image of one of the fabricated photodetectors. The HSQ cover is selectively lowered in the green rectangular area which is large enough (350 × 150 µm) to accommodate the contact pads. A 200-nm thick layer of a-Si:H was deposited by plasma-enhanced chemical vapor deposition (PECVD) using SiH_4 as a gas precursor for suitable hydrogenation of the film [18] and then patterned to reduce the interaction length with the optical waveguide to 50 µm. The two gold electrodes have a thickness of 150 nm, a width $L_e = 15$ µm, and are spaced by a distance $d = 4$ µm (note that, due to the limited resolution of the fabrication process, the length $L_d = 50$ µm of the a-Si region is longer than the region covered by the electrodes, $2L_e + d = 34$ µm).

A systematic analysis was carried out to estimate the propagation loss of the Si_3N_4 waveguide. All the results reported in this Letter refer to TE polarization. Figure 2 shows the transmission measurements on optical waveguides of increasing length at a wavelength of 660 nm. The test structures have a folded topology, like the one shown in the inset, where the length of the waveguide in the straight sections is varied, while the number and radius of the bends are kept constant. The waveguides were edge-coupled with single-mode optical fibers (mode field diameter of 3.5 µm) without using mode adapters at the chip facet. For the 400-nm wide waveguide employed for the detector, the fiber-to-waveguide coupling loss is about 10 dB/facet and the propagation loss is 1.88 dB/cm (+/– 0.1), while for a 350-nm wide waveguide a slightly higher loss (2.3 dB/cm) is observed. These results are in line with state-of-the-art values reported in the literature [9].

Figure 3(a) shows the light-dependent current measured at the two electrodes for increasing values of the optical power P_d at the input of the detector, when a constant voltage V_e is applied at the two electrodes. The reference dark current is about 25 pA at $V_e = 4$ V and 50 pA at $V_e = 8$ V, corresponding to a resistance of 160 GΩ between the electrodes. Since the transversal width of the a-Si film between the electrodes is 70 µm, this results in a conductivity of 18 nS/cm for the a-Si:H film. The dark current limits the sensitivity of the device to a minimum detectable power of –45 dBm. Above the sensitivity threshold, we observe a change of the photocurrent versus the optical power P_d across a dynamic range of more than 20 dB, the maximum power of –25 dBm being limited by the loss of the experimental setup. The responsivity R_{ph} of the device, shown in Fig. 3(b), is defined with respect to the absorbed power $P_{abs} = \eta P_d$, where $\eta = 1\text{-}\exp(-\alpha L_d)$ is the fraction of the guided light absorbed by the a-Si film. Loss measurements performed on a-Si coated test waveguides show that a 50-µm long section introduces a loss of about 2 dB, in agreement with simulations of Fig. 1(b). This means that the detector absorbs 37% of the guided light. Results in Fig. 3(a) show that, when $P_d = -30$ dBm ($P_{abs} = 370$ nW), a photocurrent of 11 nA is measured for $V_e = 8$ V, resulting in a responsivity R_{ph} of about 30 mA/W. This photocurrent essentially flows in the a-Si region on top of the waveguide that overlaps with the guided mode. Assuming a transverse width equal to that of the waveguide core (400 nm), we estimate an increase of the a-Si conductivity to 0.68 mS/cm, that is more than four orders of magnitude larger with respect to the dark level value (18 nS/cm).

Some considerations need to be made on the device responsivity R_{ph}. First, in Fig. 3(b) we see that R_{ph} remains almost constant with respect to the optical power P_d, meaning that the photocurrent increases linearly with P_d (see Supplement 1 Fig. S1 for a linear scale representation of Fig. 3(a)). This effect implies that in the considered optical power range (from –45 to –25 dBm) neither saturation effects nor carrier lifetime reduction occur, which can arise in an a-Si film exposed to a high photon flux [19]. Second, in a photoconductor the photocurrent is expected to increase linearly with the applied voltage V_e, but in the measured device when V_e is halved from 8 V to 4 V, the responsivity R_{ph} reduces by three times from about

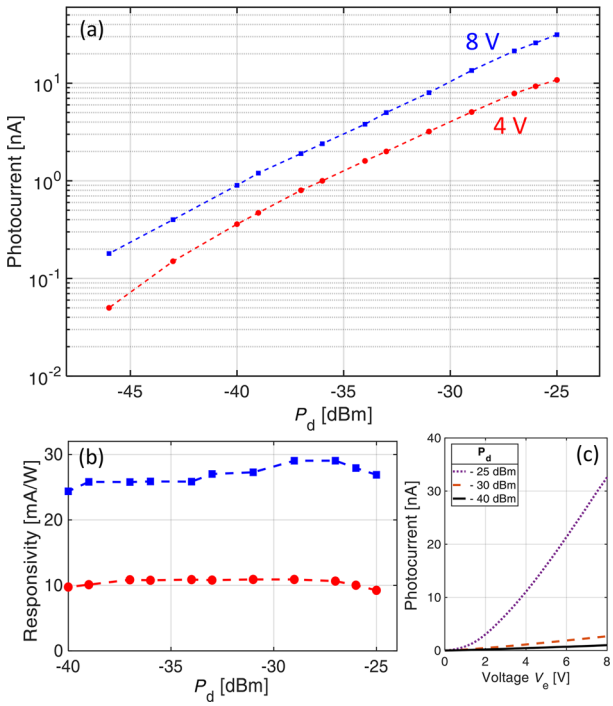

Fig. 3. (a) Measured current and (b) responsivity for increasing optical power P_d at a wavelength of 660 nm when $V_e = 4$ V (red circles) and 8 V (blue squares); (c) IV curve for increasing power P_d.

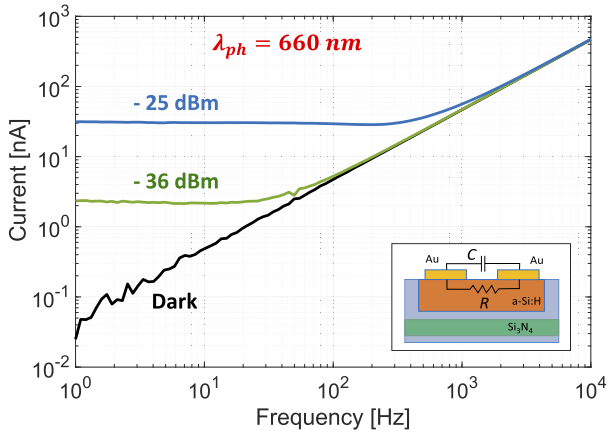

Fig. 4. Measured photocurrent versus frequency for different levels of the optical power P_d at the detector. $V_e = 8$ V, $V_{eff} = 6$ V.

30 mA/V to 10 mA/W. However, this behavior is consistent with the I-V curves of Fig. 3(c) indicating the presence of a Schottky diode at the a-Si-metal interface, with a threshold voltage $V_{th} = 2$ V. The presence of non-ohmic contacts implies that the effective voltage applied to the a-Si film in the detector region is actually $V_{eff} = V_e - V_{th}$, that is 6 V and 2 V instead of 8 V and 4 V, respectively. Regarding the carrier lifetime, in amorphous semiconductors absorption of photons with an energy higher than the material bandgap produces different kind of carriers that can contribute to the overall photocurrent. These include free carriers in the conduction and valence bands (electrons and holes, respectively) as well as trapped carriers associated with intragap defects states or surface states. In a-Si, the lifetime of trapped carriers may be orders of magnitude higher than free carrier lifetime [19]. An effective lifetime τ_{eff}, which depends on the electric field profile between the electrodes and the density of defect states [20], can be defined. The lifetime-mobility product $\mu\tau_{eff}$ is a characteristic parameter to qualify the properties of a photoconductor and can be directly derived from the responsivity R_{ph} as (see derivation in Supplement 1 Note 2)

$$\mu\tau_{eff} = R_{ph}\frac{h\nu}{q}\frac{L_d d}{V_{eff}} \quad (1)$$

where q is the electron charge, h is the Planck constant, and for simplicity we assumed a uniform electric field V_{eff}/d in the gap region between the electrodes. In our device $\mu\tau_{eff}$ is in the order of 2×10^{-8} cm^2/V (see Supplement 1 Fig. S2), in line with data reported in previous works for a-Si films [21].

The photoconductive gain G_{ph} is given by

$$G_{ph} = \frac{R_{ph}h\nu}{q} = \mu\tau_{eff}\frac{V_{eff}}{L_d d} = \frac{\tau_{eff}}{\tau_t}\frac{d}{L_d} \quad (2)$$

where $\tau_t = d^2/\mu V_{eff}$ is the transit time of the carriers though the a-Si:H film. A rather low photoconductive gain G_{ph} of about 0.05 at $V_e = 8$ V and 0.02 at 4 V (see Supplement 1 Fig. S3) is observed which is limited by both the geometrical ratio $d/L_d = 0.08$ and the time constants ratio $\tau_{eff}/\tau_t = 0.69$ at $V_{eff} = 6$ V. To quantify the magnitude of the two-time constants, we can assume a mobility μ in the order of 1 cm^2/V·s for the a-Si film [22], so that we obtain $\tau_{eff} = 18$ ns and $\tau_t = 26$ ns ($V_{eff} = 6$ V, $P_d = -30$ dBm). We expect that the photoconductive gain G_{ph} can be increased by more than one order of magnitude by reducing the electrode width to $L_e \sim 1$ µm as well as by reducing the transit time τ_t if a shorter gap d between the electrodes is realized.

To investigate the frequency-domain response of the photoconductor, we measured the change of the electrical impedance at the electrical pads of the device versus the light power P_d. The impedance measurement was performed with a lock-in detection scheme, where a sinusoidal voltage with peak value $V_e = 8$ V at a frequency f_c was applied to one electrode, while the other electrode was connected to ground. The electrical equivalent circuit of the detector is shown in the inset of Fig. 4 and consists of an RC circuit, where R is given by the a-Si film between the electrodes, while C is the parasitic capacitance between the electrodes (including the bonding wires and pads). The lock-in amplifier employed for the characterization in frequency has a minimum noise floor of 20 fA at 1 Hz integration bandwidth.

Figure 4 shows the measured AC current versus frequency f_c for increasing values of P_d. The plateau in the low-frequency side of the curves indicates the amplitude of the photocurrent flowing through the light-dependent resistance R of the a-Si:H film. In agreement with the results of Fig. 3, the photocurrent is about 30 nA for an optical power of –25 dBm while the reference dark current (black line) is less than 100 pA. At higher frequencies, all the curves asymptotically approach the straight line giving the current flowing through the parasitic capacitance C, that in the considered device is about 922 fF. This effect limits the visibility of the frequency-domain response of the detector to 1 kHz at –25 dBm.

The time-domain response of the a-Si photoconductor was assessed by using the device to detect an intensity-modulated optical signal propagating in the Si_3N_4 waveguide. The signal is generated by directly modulating a 660-nm visible-light laser source with a square wave driving current with a pulse

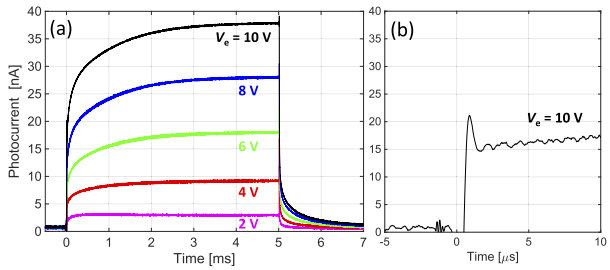

Fig. 5. (a) Time-domain response of the integrated a-Si photodetector for different bias voltages V_e. A fast response due to free-carrier dynamics (sub-μs time scale) is followed by a slower dynamics (ms-scale) due to intragap trapped carriers; (b) sub-μs time response for $V_e = 10$ V.

repetition rate of 100 Hz. The dynamics of the laser was characterized with a fast silicon photodiode with a rising time of 9 ns, showing that the rise time of the laser is about 1 μs. The readout of the a-Si photoconductor was performed with a low-noise transimpedance amplifier (TIA) providing a gain of 10^8 V/A. The output of the TIA was collected by an oscilloscope triggered by the electrical signal modulating the laser source. Figure 5(a) shows the time response of the a-Si photoconductor when $P_d = -25$ dBm for increasing voltage V_e. Two different time constants are visible in the dynamics of the device. A slower time constant, in the range of several hundreds of μs, is due to the carriers trapped in the intragap states of a-Si [23]. However, as shown in Fig. 5(b), a very fast response is observed in the first part of the transient, which is associated with the effective lifetime of free carriers τ_{eff} and is expected to occur in a time scale of several ns. In our experiment, the observation of the fast time response is limited by the rise time response of the laser (~ 1 μs) and by the limited bandwidth of the TIA that is responsible for the damping of the measured current signal.

In conclusion, we reported on an a-Si in-line photoconductor operating in the 660-nm wavelength range that is monolithically integrated with standard Si_3N_4 waveguides. The device has a sensitivity of –45 dBm, a responsivity of 30 mA/W, and a good linearity across a dynamic range of more than 20 dB (limited by the experimental setup). The time response of the device is limited to the few-ms time scale by the dynamics of intragap trapped carriers in the a-Si film, but a pronounced sub-μs response is observed that can be exploited for fast monitoring operations for the control and calibration of visible-light Si_3N_4 PICs. The size of the device (50 μm) could be downscaled by at least one order of magnitude by using higher-resolution lithography, thus leading also to a 10x improvement of the responsivity. Due to the well-assessed photogeneration properties of a-Si which extend across the entire visible-light range, the presented photoconductor concept can be extended to lower wavelengths to implement RGB detectors integrated in Si_3N_4 waveguides. Finally, the additive CMOS-compatible fabrication process makes the device concept portable to any photonic platform for visible-light applications.

Funding. H2020 Future and Emerging Technologies (829116).

Acknowledgment. This work was partially performed at Polifab, the micro- and nanofabrication facility of Politecnico di Milano (https://www.polifab.polimi.it/).

Disclosures. The authors declare no conflicts of interest.

Data availability. Data underlying the results presented in this Letter are not publicly available at this time but may be obtained from the authors upon reasonable request.

Supplemental document. See Supplement 1 for supporting content.

REFERENCES

1. W. Zixian, L. Zhongxu, L. Xin, W. Lei, W. Lai, Y. Changyuan, and H. Y. Fu, Opt. Lett. **46**, 4670 (2021).
2. J.-C. Tinguely, O. I. Helle, and B. S. Ahluwalia, Opt. Express **25**, 27678 (2017).
3. C. A. A. Franken, A. van Rees, L. V. Winkler, Y. Fan, D. Geskus, R. Dekker, D. H. Geuzebroek, C. Fallnich, P. J. M. van der Slot, and K.-J. Boller, Opt. Lett. **46**, 4904 (2021).
4. A. Mohanty, Q. Li, M. A. Tadayon, S. P. Roberts, G. R. Bhatt, E. Shim, X. Ji, J. Cardenas, S. A. Miller, A. Kepecs, and M. Lipson, Nat. Biomed. Eng. **4**, 223 (2020).
5. L. C. Moreaux, D. Yatsenko, W. D. Sacher, J. Choi, C. Lee, N. J. Kubat, R. J. Cotton, E. S. Boyden, M. Z. Lin, L. Tian, A. S. Tolias, J. K. S. Poon, K. L. Shepard, and M. L. Roukes, Neuron **108**, 66 (2020).
6. R. J. Niffenegger, J. Stuart, C. Sorace-Agaskar, D. Kharas, S. Bramhavar, C. D. Bruzewicz, W. Loh, R. T. Maxson, R. McConnell, D. Reens, G. N. West, J. M. Sage, and J. Chiaverini, Nature **586**, 538 (2020).
7. K. K. Mehta, C. Zhang, M. Malinowski, T. L. Nguyen, M. Stadler, and J. P. Home, Nature **586**, 533 (2020).
8. A. Nakao, S. Yamada, T. Katsuyama, O. Kawasaki, K. Iwabata, K. Horii, and A. Himeno, in *27th Proceedings of the International Display Workshops (IDW)* (2020), p. 649.
9. W. D. Sacher, X. Luo, Y. Yang, F.-D. Chen, T. Lordello, J. C. C. Mak, X. Liu, T. Hu, T. Xue, P. G.-Q. Lo, M. L. Roukes, and J. K. S. Poon, Opt. Express **27**, 37400 (2019).
10. W. Bogaerts, D. Pérez, J. Capmany, D. A. B. Miller, J. Poon, D. Englund, F. Morichetti, and A. Melloni, Nature **586**, 207 (2020).
11. Y. Lin, Z. Yong, X. Luo, P. G.-Q. Lo, W. D. Sacher, and J. K. S. Poon, in *Conference on Lasers and Electro-Optics (CLEO)* (2020), paper SM1A.3.
12. S. Yanikgonul, V. Leong, J. R. Ong, T. Hu, S. Y. Siew, C. E. Png, and L. Krivitsky, Nat. Commun. **12**, 1834 (2021).
13. S. Cuyvers, A. Hermans, M. Kiewiet, J. Goyvaerts, G. Roelkens, K. Van Gasse, D. Van Thourhout, and B. Kuyken, Opt. Lett. **47**, 937 (2022).
14. R. A. Street, *Hydrogenated Amorphous Silicon* (Cambridge University Press, 1991).
15. B. Desiatov and M. Loncar, Appl. Phys. Lett. **115**, 121108 (2019).
16. H. R. Philipp, J. Electrochim. Soc. **120**, 295 (1973).
17. L. Gao, F. Lemarchand, and M. Lequime, Opt. Express **20**, 15734 (2012).
18. A.T.M. Wilbers, G.J. Meeusen, M. Haverlag, G.M.W. Kroesen, D.C. Schram, and H. Kersten, Thin Solid Films **204**, 57 (1991).
19. C. R. Wronski and R. E. Daniel, Phys. Rev. B **23**, 794 (1981).
20. Y. Dan, X. Zhao, K. Chen, and A. Mesli, ACS Photonics **5**, 4111 (2018).
21. H. Okamoto, H. Kida, S. Nonomura, K. Fukumoto, and Y. Hamakawa, J. Appl. Phys. **54**, 3236 (1983).
22. R. Könenkamp, S. Muramatsu, H. Itoh, S. Matsubara, and T. Shimada, Appl. Phys. Lett. **57**, 478 (1990).
23. K. A. Conrad and E. A. Schiff, Solid State Commun. **60**, 291 (1986).